Revisiting heat treatments for additive manufactured parts: a case study of A20X alloy

Materials & Design 225 (2023) 111566

Contents lists available at ScienceDirect

Materials & Design

journal homepage: www.elsevier.com/locate/matdes

Revisiting heat treatments for additive manufactured parts: A case study of A20X alloy

Jayant Barode [a,*], Ashok Vayyala [c,d,*], Enrico Virgillito [a,b], Alberta Aversa [a], Joachim Mayer [c,d], Paolo Fino [a], Mariangela Lombardi [a]

[a] Department of Applied Science and Technology, Politecnico Di Torino, Corso Duca degli Abruzzi 24, Torino 10129, Italy
[b] Center for Sustainable Future Technologies IIT@Polito, Istituto Italiano di Tecnologia, Via Livorno 60, 10124Torino, Italy
[c] Ernst Ruska-Centre for Microscopy and Spectroscopy with Electrons (ER-C-2), Forschungszentrum Jülich GmbH, 52425 Jülich, Germany
[d] Central Facility for Electron Microscopy (GFE), RWTH Aachen University, Ahornstr. 55, 52074 Aachen, Germany

HIGHLIGHTS

- Post-processing T7 heat treatment and microstructural evolution of laser powder fused A20X alloy was investigated.
- T7 offers undissolved θ-Al_2Cu phase near TiB_2 particles and promotes early precipitate free zones formation upon aging.
- A novel short and simple heat treatment was proposed for the improved mechanical behaviour.
- Exceptional improvement (~45%) in the tensile ductility was achieved with respect to T7.

GRAPHICAL ABSTRACT

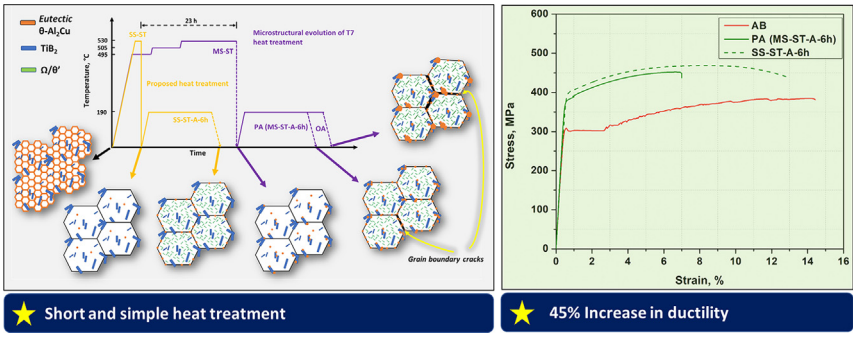

ARTICLE INFO

Article history:
Received 6 September 2022
Revised 19 December 2022
Accepted 29 December 2022
Available online 30 December 2022

Keywords:
Additive manufacturing
high strength Al alloy
Microstructural evolution
Post-processing heat treatment
Mechanical behaviour

ABSTRACT

A20X (Al-Cu-Ag-Mg-TiB_2) is a precipitation hardening alloy, recently developed for additive manufacturing processing. Printed parts of A20X alloy are usually post-processed with a long T7 heat treatment for improved mechanical properties with respect to its as-built counterparts. However, in the present investigation, it was demonstrated that T7 might not be the best suitable heat treatment available for A20X alloy. A detailed microstructural characterization of A20X samples processed with laser powder bed fusion and post-processed with T7 was carried out. Microstructural features were analysed in terms of grain size, precipitate size, phase quantification, dislocation density and width of the precipitate free zones. After the analysis, a simple and rapid heat treatment was proposed which significantly improved the mechanical properties. The yield strength (YS), ultimate tensile strength (UTS) and elongation to fracture (e) for the T7 heat treatment were 370 ± 9 MPa, 435 ± 13 MPa and 7.3 ± 0.3 % respectively. With the proposed heat treatment, an increment of 7.1 % in YS, 6.3 % in UTS and 45 % in e was witnessed. This exceptional improvement in the mechanical behaviour has been associated with the absence of grain boundary cracking in the proposed heat treatment.

1. Introduction

Additive manufacturing (AM) is a build-up process of 3D parts obtained by joining the material in a layer by layer fashion [1].

* Corresponding authors.
E-mail addresses: jayant.barode@polito.it (J. Barode), a.vayyala@fz-juelich.de (A. Vayyala).

https://doi.org/10.1016/j.matdes.2022.111566
0264-1275/

The processing conditions of additive manufacturing technique are quite different than the traditional manufacturing methods [2]. For instance, processing conditions of AM processes such as laser powder bed fusion (LPBF), directed energy deposition (DED) and electron beam melting (EBM) are characterized by the following: (i) high heating (melting) and cooling (solidifying) rates, (ii) melting of a top powder layer and consequent re-melting of an underlying solidified layer, and (iii) repeated thermal cycles of the previously deposited layers. Such a complex processing conditions in combination with materials chemistry causes various microstructural defects [2–4] which severely degrade the mechanical properties of the printed parts which were intended for structural applications. However, now it has become a common practice for the printed parts to undergo a post-processing treatments to mitigate or eliminate such microstructural defects and to modify the microstructure in order to achieve the most suitable properties [3,5].

In particular, post-processing heat treatments becomes essential if the printed parts are of a precipitation-hardening alloy [2,3,6,7]. Recently, certain precipitation-hardening Al alloys have demonstrated good processibility by AM. Among those Al alloys, A20X™ has gained quite a success and has been certified by Society of Automotive Engineers (SAE) International as a commercial alloy for aerospace application [8,9]. A20X™ is an Al-Cu-Ag-Mg alloy along with TiB_2 as a reinforcement. This composition has been developed and patented by Aeromet international limited, UK for both casting and AM processes [10,11]. The alloy benefits from the reduced hot cracking susceptibility, which is one of the major problems in the printability of precipitation hardening Al alloys by AM techniques [12] and increased strength due to the precipitation of various phases during aging [13,14].

The company (Aeromet) suggested a modified-T7 post-processing heat treatment for A20X castings [15]. This heat treatment consists of a multi-step solutioning i.e. 495 °C for 5 h + 505 °C for 6 h + 525 °C for 11 h + 538 °C for 24 h followed by artificial aging, such a long solution treatment (about 46 h) has shown a complete dissolution of Cu, which upon aging could effectively take part to the precipitation. Multi-step solution treatments are generally performed to avoid the occurrence of incipient melting in as-cast Al-Cu based alloys [16–19]. This phenomenon can be observed in such alloys due to the presence of phases with lower melting temperatures than the solutioning temperature. The occurrence of incipient melting causes the formation of micro-cracks and pores during solution treatment and degrades the mechanical properties and corrosion resistance of the material.

Due to this, multi-step solution treatments have been widely investigated [16–19]. Zamani et al. [19], utilized two-step solution treatment (490 °C for 5 h + 512 °C for 20 h) for as-cast Al-Cu-(Mg-Ag) alloy. The authors have reported that addition of Mg and Ag favours the formation of S-Al_2CuMg and Q-$Al_7Cu_3Mg_6$ phases. The S and Q phase showed their peak melting temperature in DSC profile at around 495 °C and 513 °C, respectively, and thus a two-step solution treatment could be able to dissolve these phases into the Al-matrix rather than melting. Similarly, Masuku et al., also suggested a two-step solution treatment (515 °C for 5 h + above 515 °C for 15 h) for an Al-5Cu-Mg-Ag alloy to ensure the complete dissolution of these low temperature melting phases [16]. Daswa et al. performed a comparative study between single-step (525 °C for 16 h) and multi-step solution treatment (controlled heating from 400 °C to 513 °C + 513 °C for 2 h + 525 °C for 16 h). It was reported that, a single-step solution treatment resulted in the formation of incipient melting whereas after a multi-step solution treatment no such defects were detected [18]. Similar heat treatments which were developed for castings have also been utilized for the AM printed parts. Avateffazeli et al. [20] and Shakil et al. [21] recently carried out a post-processing heat treatment similar to the modified-T7 i.e. 505 °C for 2 h + 530 °C for 4 h followed by aging at 190 °C for 4–6 h, and compared their bulk- and micro-mechanical properties with the as-built A20X counterparts. Both studies have reported an increase in the strength after T7 heat treatment compared to their as-built counterparts.

However, a detailed study on the microstructural evolution and the effects of a T7 heat treatment on additively manufactured A20X alloy has not yet been reported. It is well known that the processing conditions differ significantly between the casting and AM and so does their microstructural features. Thus, heat treatments which are specific to the microstructural features should be redesigned to exploit the full potential of the materials performance for the intended applications such as mechanical behaviour, corrosion resistance etc. In the present study, a detailed investigation of the microstructural evolution during the T7 heat treatment of the A20X alloy processed by LPBF is presented. The outcome of the work has paved the way to the design of a more promising heat treatment.

2. Materials and methods

A gas atomized A20X powder provided by ECKART and ALTANA Company was used for printing bulk samples. The composition of the powder, provided by the supplier, is presented in Table 1. The powder particles size distribution (PSD) was evaluated by image analysis of at least 20,000 particles using a Phenom XL table-top Scanning Electron Microscope (SEM).

Parallelepipeds samples (12x10x10 mm^3) were printed by LPBF process using an EOS M270 dual mode system. The optimized parameters employed for printing are presented in Table 2. These parameters were optimized after density measurements. The printing process was performed in an argon atmosphere, platform was pre-heated to 100 °C, and rotated scanning strategy was 67°.

The post-processing multi-step solution treatment (MS-ST) was performed in a horizontal tubular furnace (Nabertherm RHTC 80–710/15) under argon atmosphere, followed by water quenching (WQ) at room temperature. Various interrupted solution treatments were also performed to track the microstructural evolution. The details and the nomenclature of these heat treatments are presented in Table 3. Aging was carried out in an oven at 190 °C for various intervals of time, followed by air cooling. The steps of the heat treatment are presented as a schematic in Fig. 1.

Metallographic sample preparations were performed by polishing according to the standard metallographic procedure and by etching with Keller's reagent for 5 s. Microstructural characterizations were performed using an optical microscope (Leica DMI 5000 M), a Phenom XL table-top Scanning Electron Microscope (SEM) and a TESCAN S900 Field Emission Scanning Electron Microscope (FESEM) equipped with Secondary Electron (SE), Back Scattered Electron (BSE) detectors and an Energy Dispersive Spectroscopy (EDS). Electron backscattered diffraction (EBSD) was performed using 20 kV and 10nA with a step size of 0.2 μm. Transmission electron microscopy (TEM) characterizations were done on a very thin lamella of thickness close to 100 nm prepared from bulk samples using a Helios NanoLab 460 F1 dual beam FIB-SEM equipped with Ga + ion source. A step-by-step procedure for preparing a damage-free lamella can be found elsewhere [22]. High-angle annular dark-field (HAADF) STEM imaging and corresponding EDX chemical mappings were performed using an FEI Titan G2 80–200 ChemiSTEM microscope at 200 kV, equipped with a high-brightness field-emission gun, a probe Cs corrector, and a super-X energy-dispersive X-ray spectroscopy system [23]. The convergence semi-angle for STEM imaging was ~ 25 mrad, and the collection semi-angle was 80–200 mrad. The microstructural

Table 1
Nominal composition of the A20X powder.

	Cu	Mg	Si	Fe	Ag	B	Ti	Al
wt. %	4.20–5.00	0.20–0.33	< 0.1	< 0.08	0.60–0.90	1.25–1.55	3.00–3.85	Balance

Table 2
LPBF optimized process parameters for A20X alloy.

Parameter	Value
Laser power	195 W
Scan speed	800 mm/s
Hatching distance	0.13 mm
Layer thickness	30 μm
Volumetric energy density	62.5 J/mm^3

Table 3
Various post-processing heat treatments performed on A20X.

Heat treatment	Temperature and Time
ST-A	300 °C for 4 h
ST-B	400 °C for 4 h
ST-C	495 °C for 4 h
ST-D	495 °C for 4 h + 505 °C for 6 h
MS-ST	495 °C for 4 h + 505 °C for 6 h + 530 °C for 12 h
SS-ST	530 °C for 1 h
Aging	190 °C for 2, 4, 6, 8 and 10 h

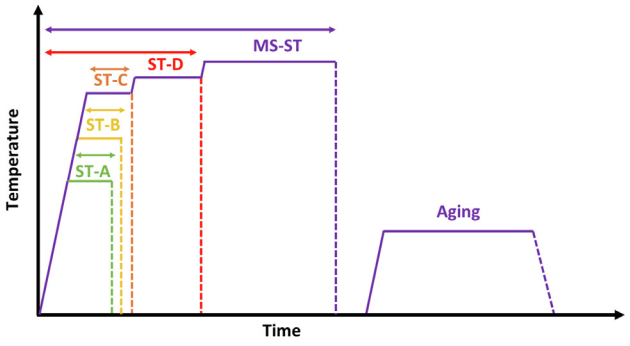

Fig. 1. A schematic representation of various heat treatments performed on the as-built A20X alloy.

features observed by various characterization techniques were quantified using an ImageJ 1.53 k software.

Phase analysis was carried out by X-ray Diffraction (XRD) in a Panalytical X'Pert PRO PW 3040/60 X-ray diffractometer using a monochromatic Cu-Kα radiation of 1.54 Å operated at 40 kV and 40 mA with a step size of 0.013° and 25 s. per step. Individual peak profiles were obtained with a step size of 0.007° and 30 s per step. Phase quantification was performed by Rietveld refinement method using Panalytical X'Pert Highscore Plus software. The refined parameters were phase scale factor, specimen displacement, unit cell, peak broadening factors (U, V and W), peak shape factor and preferred orientation coefficient. Instrumental broadening was obtained from the spectrum of LaB_6 standard sample. Dislocation density was calculated by XRD line profile analysis using the Williamson-Hall (W-H) plot [24,25].

Differential scanning calorimetry (DSC) curves were obtained using NETZSCH DSC 214 Polyma. The DSC samples were weighed around 15 mg and were heated from 27 °C to 550 °C at 10 K/min in N_2 atmosphere. Micro-hardness values were obtained with a micro-Vickers Leica VMHT indenter using 100 g load and 15 s of dwell time (10 measurements/sample). Tensile tests were performed by Zwick-Roell ProLine Z0505 with 8×10^{-3} s^{-1} as strain rate, on samples of ASTM E8 standard dimension.

3. Results and discussion

3.1. A20X powder characterization

The A20X powder morphology, microstructure and phase analysis were characterized by SEM and XRD as shown in the Fig. 2. The SEM micrograph **(in** Fig. 2**a)** shows that the particles were mostly spherical and accompanied by fine satellites. The PSD shows a unimodal distribution with D_{10}, D_{50} and D_{90} as 21 μm, 30.6 μm and 49.8 μm, respectively (see Fig. 2**b**). The microstructure of the particles from cross-sectional view revealed a cellular structure, where the cell boundaries are enriched with eutectic θ-Al_2Cu whereas the cells are composed of α-Al matrix, which can be clearly seen in Fig. 2**c**. The θ-Al_2Cu as cell boundaries was formed as a result of an eutectic reaction ($Al_{(liq)} \rightarrow$ α-$Al_{(s)}$ + θ-$Al_2Cu_{(s)}$) [26,27]. The micro-TiB_2 particles were also observed to be present at the cell boundaries, within the cell as well as at the cell triple junctions. These phases were also detected by XRD as shown in Fig. 2**d**.

3.2. Microstructural evolution during T7 heat treatment

The micro-hardness values of as-built (AB) and heat-treated samples are shown in a histogram in Fig. 3. The hardness values were reduced from AB (≈113 HV) to MS-ST (≈103 HV) state. During aging at 190 °C, the micro-hardness values exhibited a typical gaussian curve, where the peak hardness (about 152 HV) was achieved after 6 h, designated as peak aged (PA) state. Continue aging to 10 h reduced the hardness value to 124 HV, designated as over aged (OA) state. To have a better understanding of the salient microstructural features responsible for the peak hardness, the microstructural investigation was carried out using SEM (Fig. 4) and EBSD (Fig. 5) for all 4 different stages: AB, MS-ST, PA and OA.

The AB microstructure showed a typical cellular structures of additively manufactured A20X alloy as reported elsewhere [20,27,28]. The cross-sectional SEM-BSE micrograph of the AB sample revealed a well-defined cellular microstructure having cell boundaries enriched with θ-Al_2Cu and α-Al cells along with elongated micro-TiB_2 particles as shown in Fig. 4**a**. The AB microstructure was found to possess similar microstructural features to the as-atomized powder (Fig. 2**c**). However, unlike in the A20X powder, where θ-Al_2Cu formation happens solely by eutectic solidification, in the AB samples, the θ-Al_2Cu phase could be formed in two different ways, majorly as a eutectic product during solidification (cell boundary) and partially as a precipitate by a solid-state process. The precipitation could occur due to multiple thermal cycles experienced by previously solidified layers which are supersaturated with Cu due to the rapid solidification [29].

After MS-ST, the eutectic network of θ-Al_2Cu disappeared (Fig. 4**b**). The micro-TiB_2 particles were observed majorly at the grain boundary triple junctions or along the grain boundaries. There are also few θ-Al_2Cu precipitates spotted at the micro-TiB_2 particles, see supplementary Fig. S1**b**. Upon aging, the solutionized Cu precipitated out of the matrix as θ-Al_2Cu phase near micro-TiB_2 particles and at the grain boundaries, Fig. 4**c** and Fig. S1**c**. The precipitation of θ-Al_2Cu at the micro-TiB_2 particles can be attributed to

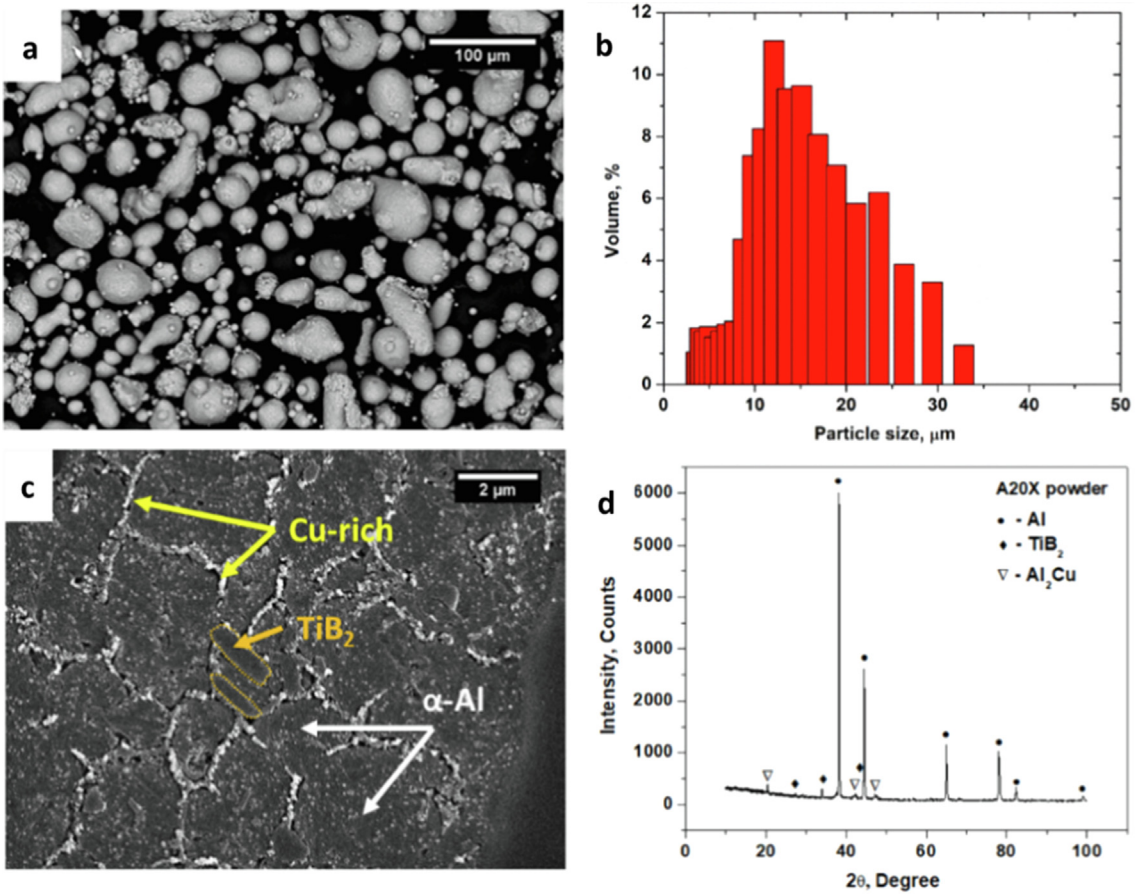

Fig. 2. A20X powder characterization showing (a) powder morphology, (b) volume particles size distribution, (c) particle cross-sectional microstructure and (d) XRD phase analysis.

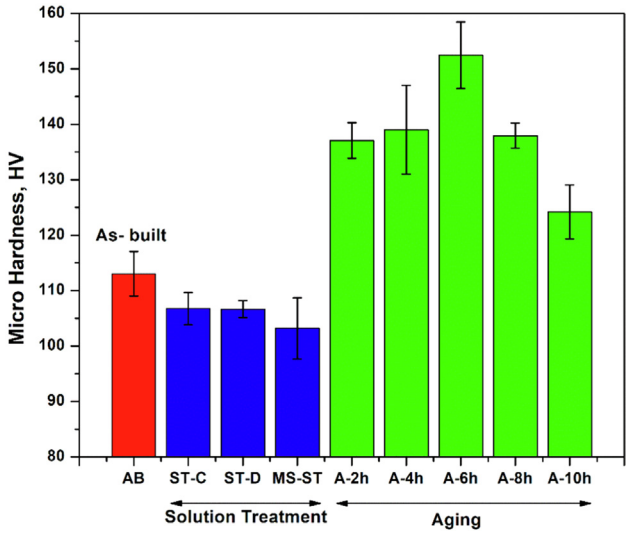

Fig. 3. Evolution of micro-hardness of A20X during MS-ST and subsequent aging.

the differences in the thermal expansion coefficient (α) of Al (26.5×10^{-6} K^{-1}) and TiB_2 (7.7×10^{-6} K^{-1} along c-axis and 4.1×10^{-6} K^{-1} along a-axis). Because of this difference, upon quenching, dislocations are trapped at the vicinity of TiB_2-Al interface [30–32]. During aging, Cu atoms diffuse through these high dislocation density channels by pipe diffusion mechanism and accelerate the nucleation and growth of θ-Al_2Cu precipitates at the TiB_2 particles [30,31,33,34]. Excessive aging i.e. OA (190 °C for 10 h) significantly enhanced the size of θ-Al_2Cu precipitates, which nearly engulfed the micro-TiB_2 particles, Fig. 4**d and** Fig. S1**d**. In the OA state, it was difficult to clearly distinguish between θ-Al_2Cu and micro-TiB_2 particles even under low brightness (Fig. S1**d**). Surprisingly, some grain boundary cracks were also noticed in the PA state (yellow arrow in Fig. 4**c**). These cracks were more frequent and severe in the OA state. No such cracks were observed in the AB state and thus their origin is likely to be related to the post-processing heat treatment.

Fig. 5 shows the EBSD scans of the 4 states. The grain size in AB state was estimated to be 1.05 µm (Fig. 5**a**). Moreover, it was observed that, the cell size is equivalent to the grain size. Unindexed black interconnected patches surrounding the grains are likely to be of eutectic θ-Al_2Cu phase. After MS-ST, the grain size grew twice to that of the AB state (≈ 1.97 µm) (Fig. 5**b**). However, it is important to note that there is no significant increase in the grain size after such a long solution treatment (nearly 24 h). This limited grain growth can be attributed to the Zenner pinning effect by the micro-TiB_2 particles at the matrix grain boundaries [35]. The average grain size in the PA (2.16 µm) and OA (1.93 µm) states are almost similar to that of MS-ST state **(**Fig. 5**c and** Fig. 5**d)**.

The phase analysis was carried out by XRD (Fig. 6). The XRD diffractogram of AB, MS-ST, PA and OA revealed primarily-three phases: Al, TiB_2 and θ-Al_2Cu, see Fig. 6**a**. The individual peak profiles of θ-Al_2Cu (1 1 0) and Al (1 1 1) phases are shown in Fig. 6**b and** Fig. 6**c**, respectively. The increase in the intensity of θ-Al_2Cu peak during aging is depicting θ-Al_2Cu precipitation and coarsening. A quantitative estimation of the phase evolution from the AB

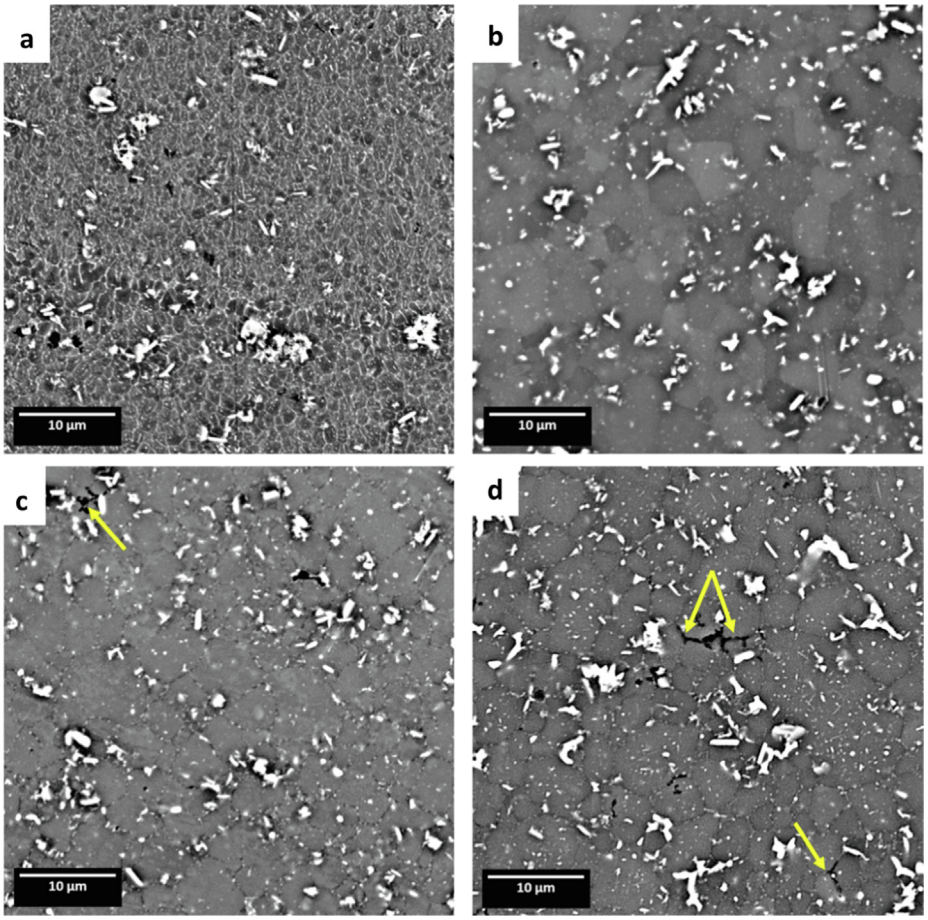

Fig. 4. SEM-BSE micrographs of A20X samples in the (a) AB, (b) MS-ST, (c) PA and (d) OA states *(Yellow arrows depict grain boundary cracks).*

to the OA state was performed by Rietveld method and is presented in Fig. 6**d**. The θ-Al_2Cu phase in the AB state was quantified to be 4.23 wt%. The phase quantification in the MS-ST state was not carried out due to its very low peak-to-background ratio of the θ-Al_2Cu phase, it would avoid the error in quantification during peak fitting. The θ-Al_2Cu phase content in the PA state increased to 1.95 wt% which then significantly increased to 4.20 wt% in the OA state, this is in line with the observation made from SEM micrographs (Fig. 4). The phase quantification of TiB_2 was around 5.5 wt % in all the states.

The individual peak profiles of Al (1 1 1) showed a shift towards higher 2θ values after MS-ST with respect to its reference position (dotted line). This peak shift corresponds to a decrease in its lattice parameters as a result of solid solution by Cu [36]. Interestingly, peak broadening of the Al phase during aging was observed, see Fig. 6**c**. For instance, the average full-width at half maximum (FWHM) of Al (1 1 1) peak in AB, MS-ST, PA and OA are 0.106°, 0.088°, 0.096° and 0.094° (2θ), respectively. The dislocation density in Al matrix associated with the peak broadening was obtained by W-H plot and the values are presented in Fig. 6**e**. The AB state possessed a high dislocation density of $6.13 \times 10^{14}/m^2$, which is a typical characteristic of additively manufactured Al alloys [37]. The dislocation density decreased after MS-ST ($2.63 \times 10^{14}/m^2$) but then increased again substantially in the PA (5.34×10^{14} $/m^2$) and OA (4.12×10^{14} $/m^2$) states.

In order to understand the origin of such high dislocation densities during aging, DSC profiles were investigated and the sequence of precipitation and phase evolution were analysed (Fig. 7). Majorly 3 peaks were detected in AB and MS-ST specimen as shown in Fig. 7**a**. The first peak was an endothermic peak which belongs to the dissolution of GP zones or Mg-Ag co-clustering [38]. The second peak was a large and broad exothermic peak, corresponding to the precipitation and the third peak was also a broad endothermic peak, depicting dissolution of all the precipitates [39].

By comparing the DSC curves, it indicates that the GP zone dissolution in the MS-ST occurred at much lower temperature and possessed larger area under the peak with respect to the AB state. This has been attributed to the dissolution of a larger volume fraction of smaller GP zone in MS-ST state with respect to the AB state [40]. The MS-ST sample displayed the largest area of the exothermic peak i.e. highest amount of precipitation. However, the broadness of the peak indicates that the process of precipitation was not a single event but occurred over a span of temperatures. On deconvolution, 3 sub-peaks were identified as shown in Fig. 7**b**. Their peak temperatures were about 230 °C, 260 °C and 310 °C which correspond to the precipitation of Ω & θ'', θ' and θ phase, respectively [38,39,41].

Although, DSC hints the formation of multiple precipitates, the resolution of SEM was not sufficient to resolve these precipitates. Therefore, high resolution STEM was used for this. The STEM-EDS mapping (Fig. 8) of the PA state showed fine and discontinuous grain boundary precipitates (Fig. 4). These precipitates were enriched with Cu and accompanied by nano-TiB_2 particles. It was suspected that these precipitates are likely to be of an equilibrium θ-Al_2Cu and might have nucleated due to the difference in CTE of Al and TiB_2 as discussed previously. Additionally, Mg segregation at grain boundaries was also observed. Within the grains, a large number of needle-shaped precipitates, which are of nanosized

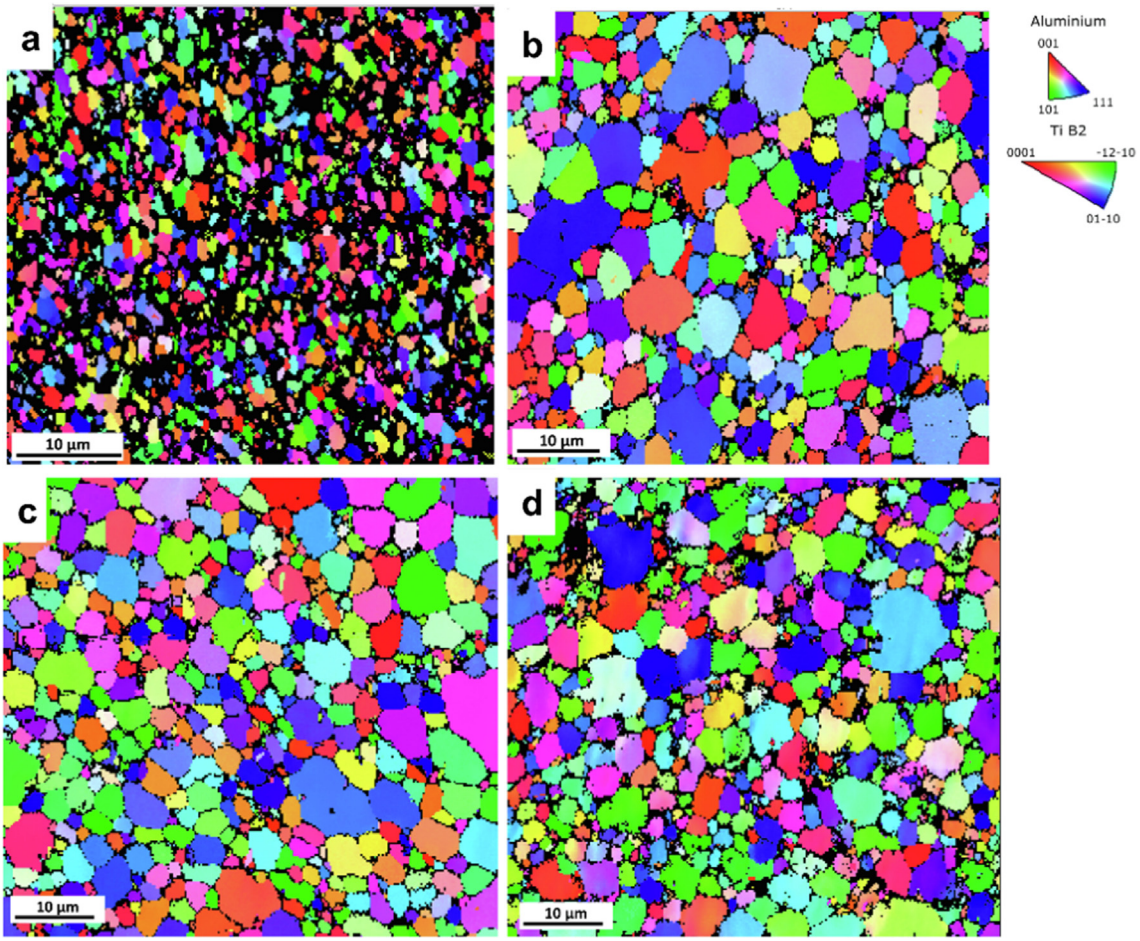

Fig. 5. EBSD micrographs showing evolution of grain structure in various conditions (a) AB, (b) MS-ST (c) PA and (d) OA.

(about 52 nm in length) (Fig. S2**a)** and enriched with Cu but also partly enriched with Ag and Mg were observed **(**Fig. 8**)**. These needle-shaped precipitates seem to hold an orientation relationship with the Al-matrix. Three different orientations within a single grain could be detected. According to the earlier researchers, these precipitates are most likely to be of coherent Ω-Al_2Cu and semi-coherent θ'-Al_2Cu [20,21,42]**.**

The Ω and θ' precipitates prefer to nucleate at the Al {1 1 1} and {0 0 1} planes, respectively. These phases possess the same chemical composition of an equilibrium θ-Al_2Cu phase [42]. Both Ω and θ' phase can be generated from a supersaturated solid-solution (SSSS) by two independent precipitation sequences [43]:

SSSS → G.P. Zone (Cu) → θ'' →θ' on $\{001\}_\alpha$ → θ.

SSSS → G.P. Zone (Mg and Ag) → Ω on $\{111\}_\alpha$ → θ.

However, precipitation of Ω phase is more favourable than θ' in Al-Cu-Ag-Mg alloys because of Mg and Ag co-clustering, which reduces the interfacial energy for the precipitating nuclei at coherent $\{111\}_\alpha$ habit planes and moreover facilitates the nucleation of the Ω which are coherent with Al matrix [14,44,45]. The Ω and θ' phases are considered as the predominant hardening phases however, Ω-plates offers much higher strength when exposed to higher temperatures or for longer aging times due to higher coarsening resistance than θ' [42,45–48]. Thus, few large matrix precipitates (of size ≈ 420 nm) which were observed in the OA state might be of θ', (see the inset Fig. S2**b**). Nonetheless, there is a large lattice misfit associated with these coherent-Ω and semi-coherent-θ' precipitates with the Al matrix and this gives rise to micro-strains upon precipitation [49–52]. Thus, a high density of Ω and θ' precipitates results in large micro-strains which are directly linked to the presence of high dislocation densities in the PA and OA state. Hence, these precipitates are responsible for peak broadening which was evident in the XRD diffractograms as shown in Fig. 6**c and** Fig. 6**e**.

From the present microstructural evolution analysis, the distinctive features which are responsible for the peak hardness after 6 h of aging are presence of dense coherent-Ω and semi-coherent-θ' nano-precipitates within the matrix, optimum precipitation θ-Al_2Cu (OA state significantly coarsened θ-Al_2Cu) and less frequent grain boundary cracks with respect to the OA state.

3.3. Grain boundary cracking during aging

During aging, the microstructural characterization revealed grain boundary cracking in both PA and OA states. Grain boundary cracking can be related to the synergetic effect of (i) development of micro-strains (dislocations) **(**Fig. 6**e)** during aging due to the presence of coherent (Ω-Al_2Cu) and semi-coherent (θ'-Al_2Cu) nano-precipitates and (ii) simultaneous increase in the width of precipitate free zones (PFZs) at the vicinity of grain boundaries and micro-TiB_2 particles (Fig. 9).

The process of precipitation and growth during aging results in the creation of PFZs in the vicinity of specific microstructural features. From the PA to the OA state, the PFZs width near grain boundaries increased from 30 nm to 85 nm (Fig. 9**b and** Fig. 9**d**) whereas PFZs width near micro-TiB_2 particles increased from 78 nm to 153 nm (Fig. 9**a and** Fig. 9**c**). It should be noted that in both PA and OA states, the PFZs width near micro-TiB_2 particles was much larger than near grain boundaries. Widening of PFZs

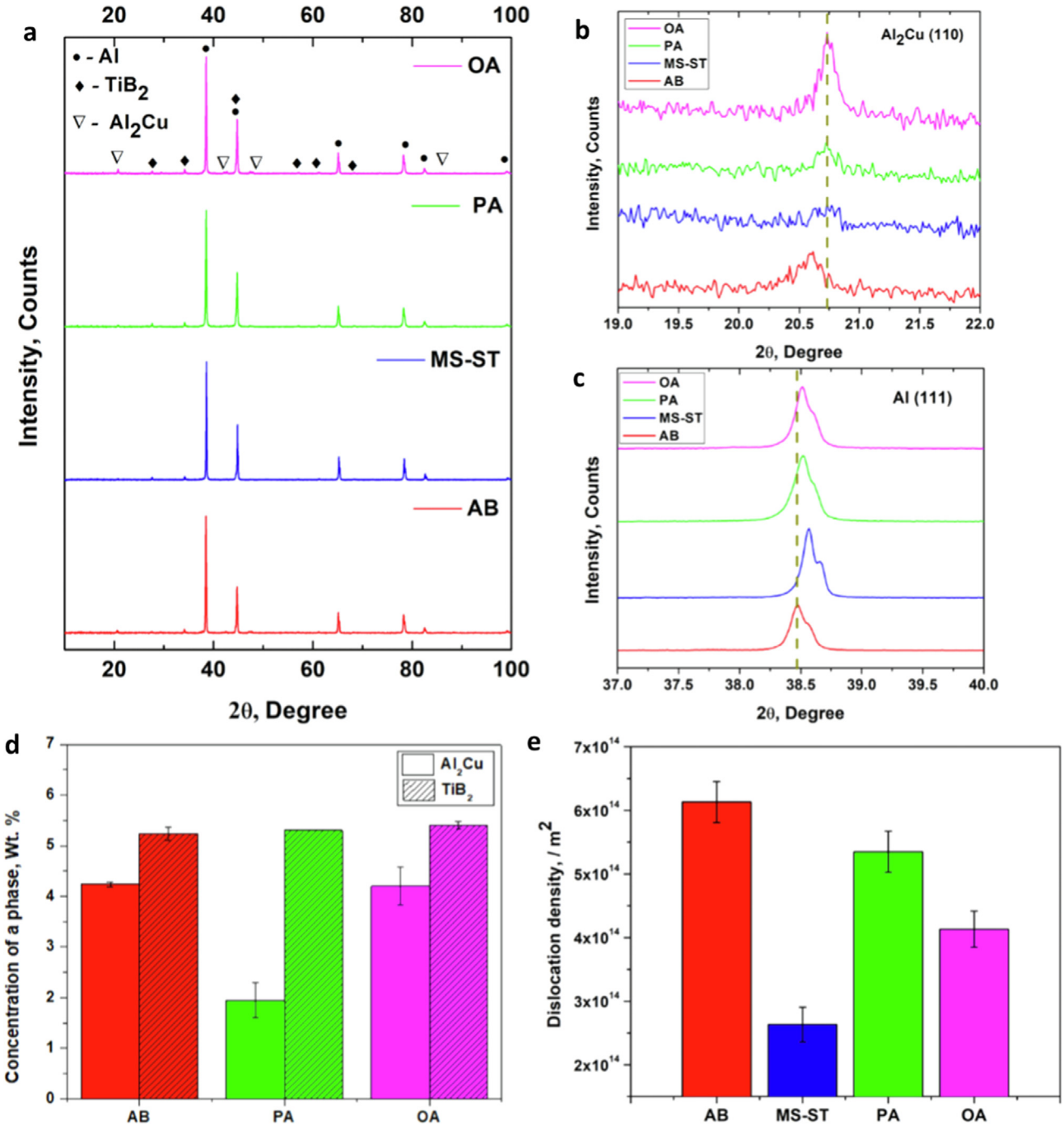

Fig. 6. (a) Phase identification by XRD measurements of AB, MS-ST, PA and OA state; individual peaks profiles of (b) Al_2Cu (1 1 0) and (c) Al (1 1 1); (d) quantification of θ-Al_2Cu and TiB_2 phases calculated by Rietveld refinement and (e) an estimated dislocation density by W-H plot. *(Reference code for the phases, goodness of fit and weighted R profile values of the refinement are provided in the supplementary file,* ***Table S1****).*

has a direct correlation with the growth of precipitates at these locations. The grain boundary precipitates present at the nano-TiB_2 particles did not show any considerable increase in their size, whereas θ-Al_2Cu precipitates near micro-TiB_2 particles grew immensely from the PA to OA state and thus consumed higher amounts of solute atoms within its vicinity leading to larger PFZs width.

The precipitation of coherent-Ω and semi-coherent-θ' during aging could generate micro-strains, resulting hardening of the grain interiors. The development of micro-strains within the matrix was evident by the presence of high dislocation densities. This results in the localized deformation near the grain boundaries and might induce grain boundary cracking [53], popularly known as strain-age cracking and is generally observed during the post weld heat treatment of superalloys [53–55]. Moreover, this effect is quite severe if there exists PFZs near grain boundaries and at triple junctions [53]. The localized deformation at the PFZs can cause the nucleation of cracks which can easily propagate along the PFZs leading to grain boundary cracking [56,57].

3.4. Microstructural evolution during multi-step solution treatment (MS-ST)

Upon aging, the material experiences cracks formation, which has been correlated with the increase in PFZs width due to significant growth of θ-Al_2Cu at micro-TiB_2 particles. In order to under-

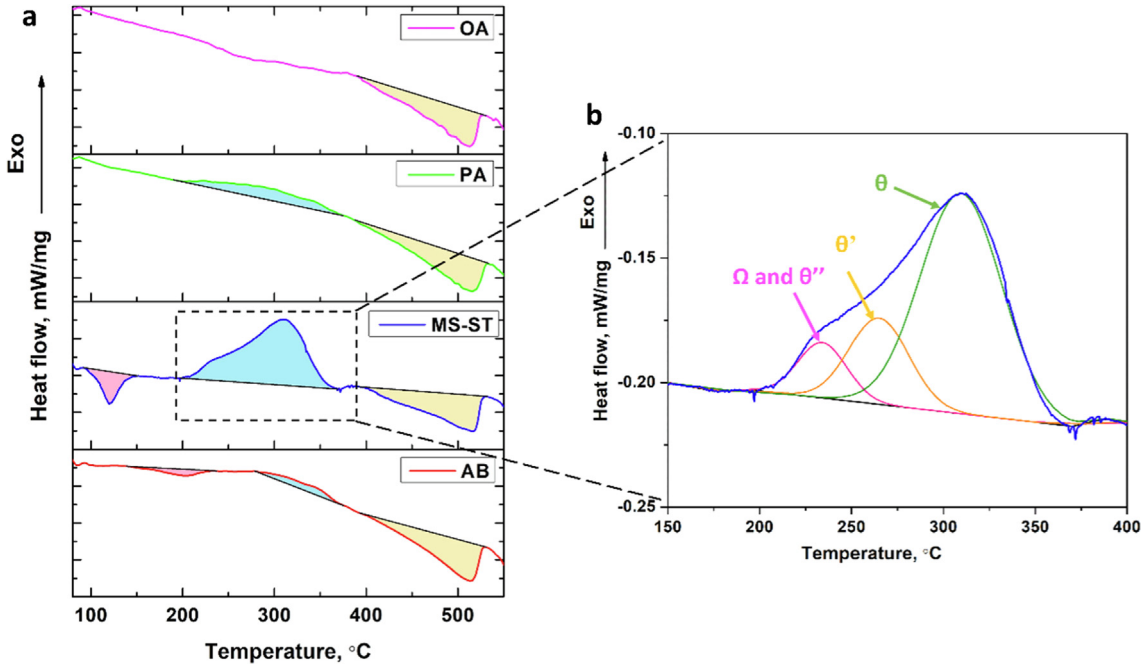

Fig. 7. (a) DSC curves of AB, MS-ST, PA and OA states and (b) deconvolution of the broad exothermic peak of MS-ST state.

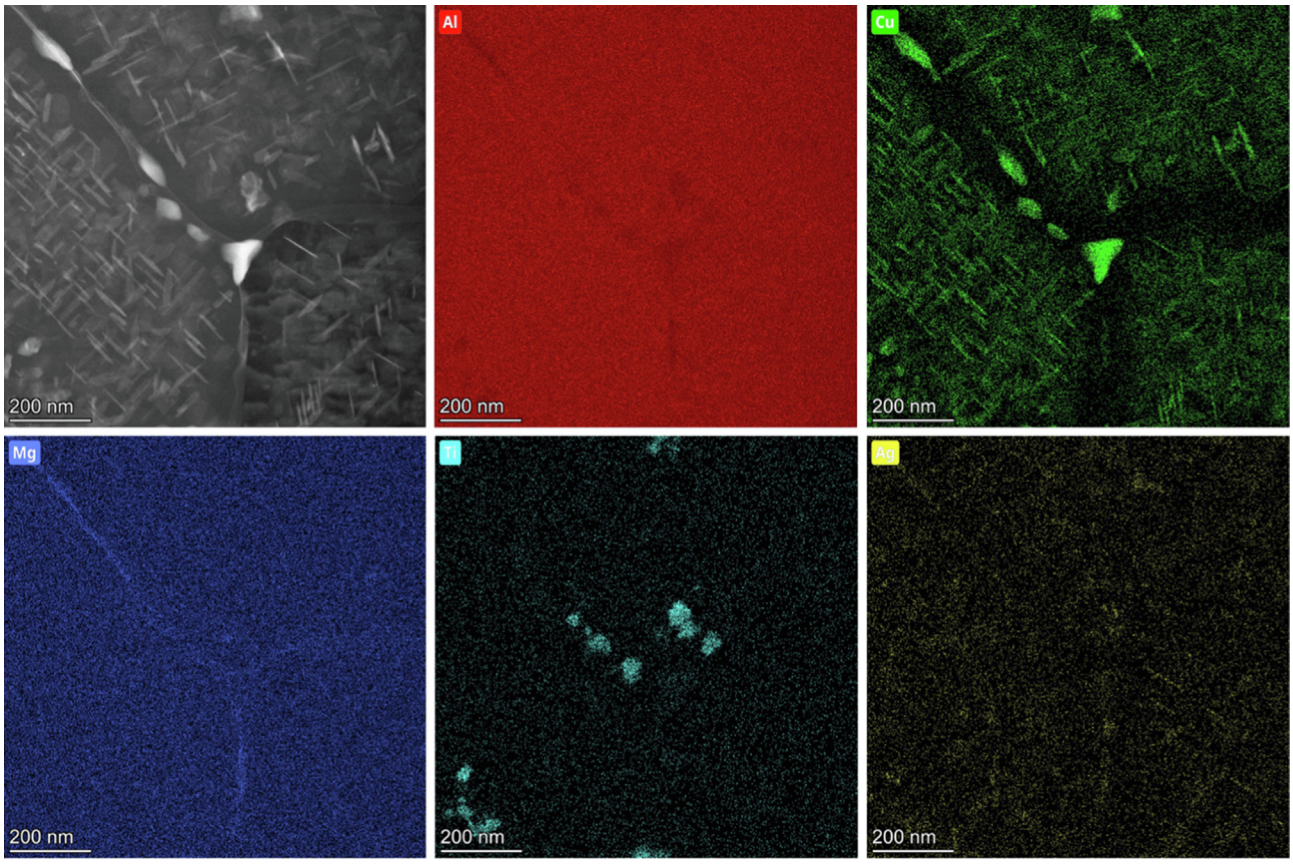

Fig. 8. High resolution HAADF-STEM micrograph and corresponding EDS mapping of a grain boundary triple junction in the PA state.

stand, if the multi-step solution treatment (MS-ST) has any role on this particular aging behaviour, evaluations of the microstructure at various solution steps were performed.

SEM micrographs were taken using backscattered electrons (BSE) mode with both high and low brightness values (Fig. 10 **(a-f and a'-f')**). These different image settings were used to distin-

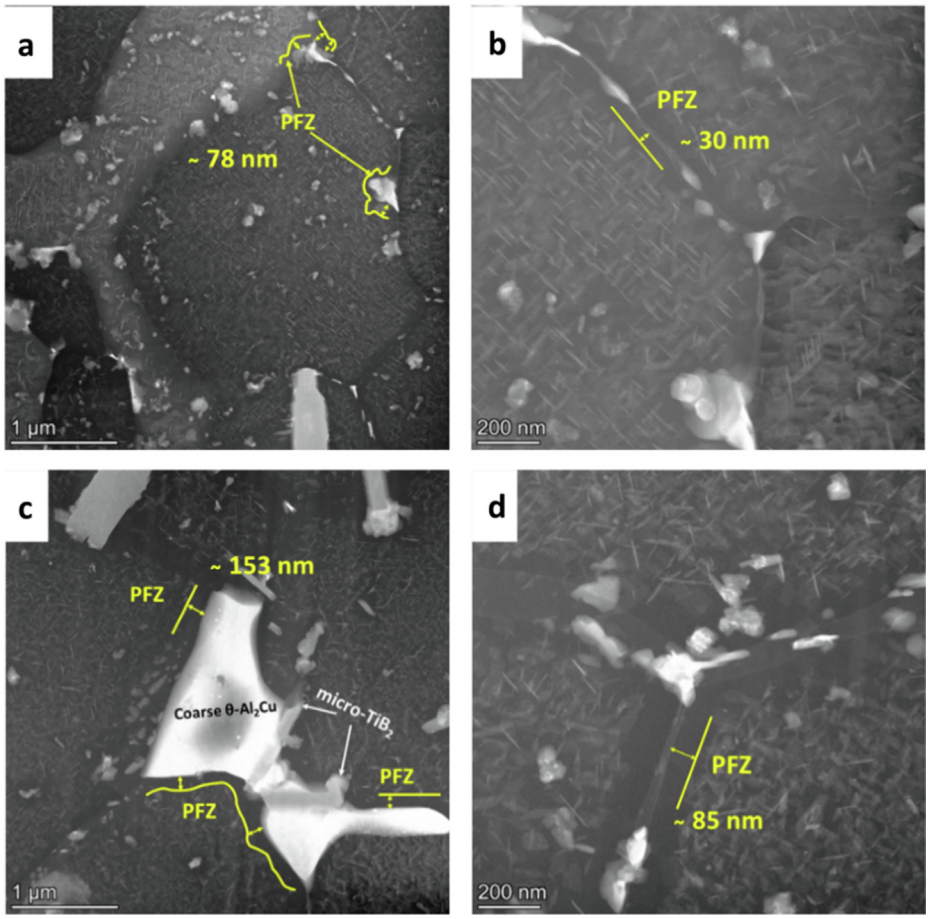

Fig. 9. High resolution HAADF-STEM micrographs indicating the PFZs in PA (a-b) and OA (c-d) state near micro-TiB_2 particles and grain boundaries.

guish TiB_2 (grey) and θ-Al_2Cu (white) phases by atomic contrast. These micrographs were used to quantify the microstructural features of θ-Al_2Cu in terms of area equivalent average-radius (r), circularity (C), number density and inter-precipitate spacing (λ) as shown in Fig. 11.

Heating the AB sample **(**Fig. 10**a and** Fig. 10**a')** to ST-A (300 °C for 4 h) leads to breaking up of the cellular structure as observed in Fig. 10**b and** Fig. 10**b')**. The eutectic θ-Al_2Cu network fragments into fine spherical particles (r = 73 nm, C = 0.87). The microstructure was also characterized by high number density of θ-Al_2Cu particles (0.21/µm^2) and low inter-precipitate spacing (λ = 0.99 µm) (Fig. 11). These fine fragmented particles could then be able to spheroidize by the Rayleigh instability process which occur by the diffusion of atomic species such as Al and Cu from their edges towards the flat surface due to capillary forces [58,59].

After the ST-B heat treatment (400 °C for 4 h), the spheroidized θ-Al_2Cu eutectic particles were happened to be of a larger size (r = 251 nm) than the ST-A ones. They appeared to be migrated towards micro-TiB_2 particles, as seen in Fig. 10**c and** Fig. 10**c'**. The migration of θ-Al_2Cu eutectic towards TiB_2 particles has been attributed to the process of Ostwald ripening due to difference in the CTE of Al and TiB_2 and generation of localized dislocation density [60]. The Ostwald ripening was also quantitatively reflected by the significant increase in average size of θ-Al_2Cu from 73 nm to 251 nm (Fig. 11**a)** and a considerable decrease in the average number density from 0.21 /µm^2 to 0.09 /µm^2 (Fig. 11**b)**. The migrated θ-Al_2Cu at micro-TiB_2 particles further coarsened during the ST-C heat treatment (495 °C for 4 h) (Fig. 10**d and** Fig. 10**d')**, reaching the maximum average size of r = 310 nm **(**Fig. 11**a)**.

After the ST-D heat treatment (495 °C for 4 h + 505 °C for 6 h), the microstructure showed both fine and coarse θ-Al_2Cu precipitates, which demonstrated that certain θ-Al_2Cu precipitates were dissolved back into the matrix (Fig. 10**e and** Fig. 10**e'**). The temperature (505 °C) utilized in ST-D heat treatment was reported to initiate the dissolution of θ-Al_2Cu [19].

Finally, the very long MS-ST (495 °C for 4 h + 505 °C for 6 h + 530 °C for 12 h) which was specifically reported to completely dissolve the large blocky θ-Al_2Cu precipitates in castings of Al-Cu based alloys [61,62], could not be able to completely dissolve the θ-Al_2Cu precipitates in the present case, especially at micro-TiB_2 particles, see Fig. 10**f and** Fig. 10**f'**. Overall, upon the MS-ST, the average number density of θ-Al_2Cu significantly reduced and the inter-precipitates spacing increased and reached a value (λ = 2.5 µm) almost equivalent to the average grain size of MS-ST.

The incomplete dissolution of θ-Al_2Cu phase even after long MS-ST could be attributed to the shielding effect of micro-TiB_2 particles which reduce the contact area between θ-Al_2Cu and Al-matrix and greatly limit the dissolution rate [63]. A similar phenomenon was described by Asghar et al. in AlSi12Ni alloy, where 3D interconnectivity of rigid Ni-aluminides with eutectic Si retarded the spheroidization of Si [64]. Recently, Zamani et al. [61], demonstrated that interconnectivity of the TiB_2 and Al_2Cu retards the diffusivity of Cu atoms along grain boundaries and at Al_2Cu/α-Al interface. This phenomenon was modelled by reducing the effective diffusion coefficient of Cu in Al to 2–2.5 times than its typical value.

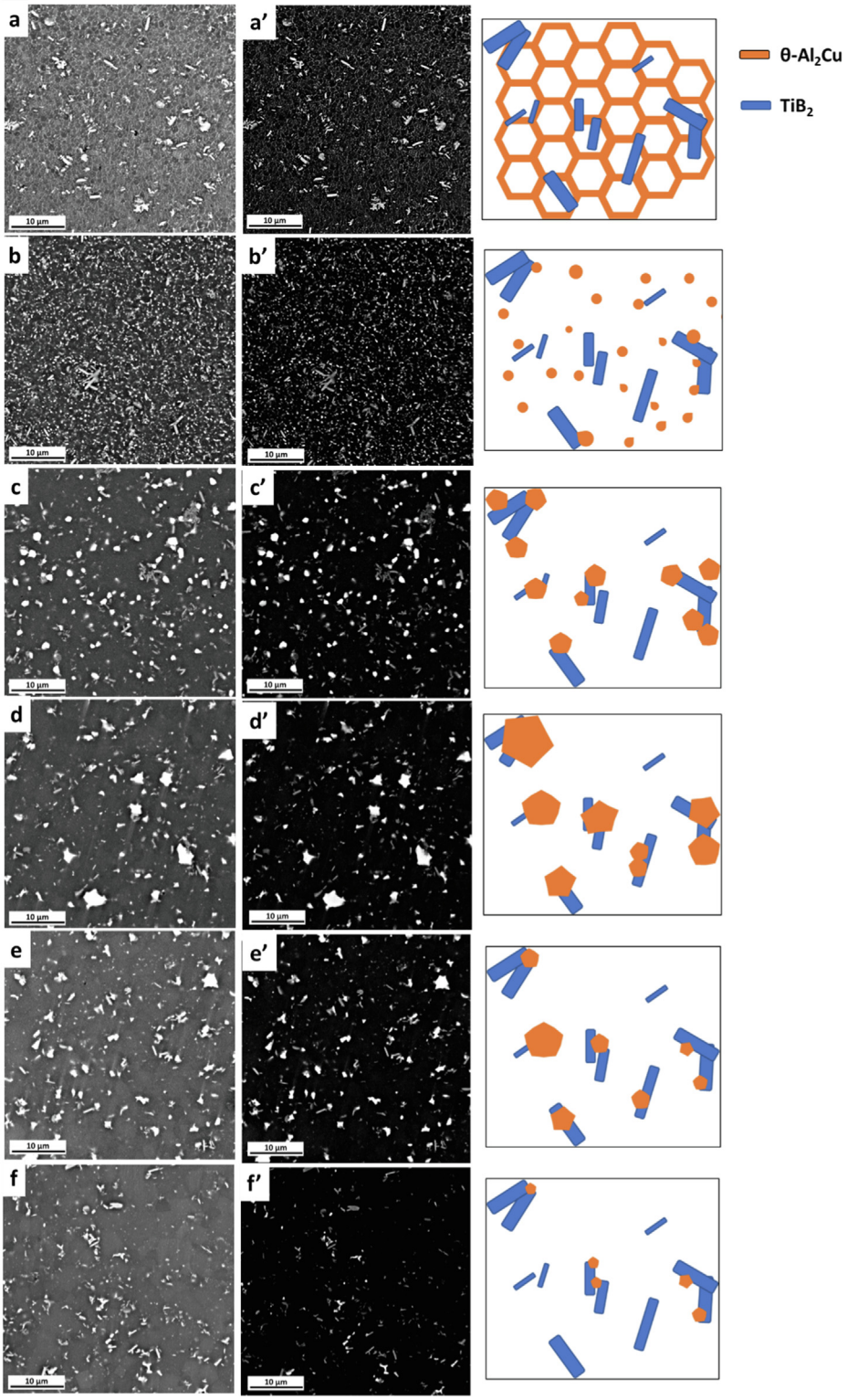

Fig. 10. SEM-BSE micrographs under high (a-f) and low (a'-f') brightness showing microstructural evolution at various interrupted steps during solution treatment. (a and a') AB, (b and b') ST-A, (c and c') ST-B, (d and d') ST-C, (e and e') ST-D and (f and f') MS-ST. (*TiB_2 particles as grey and θ-Al_2Cu as white).* A schematic view of the corresponding microstructure (on the right-hand side) is shown for each interrupted step.

3.5. A comparison of multi-step (MS-ST) and single-step (SS-ST) solution treatments

As previously described, since the MS-ST microstructure serves as an initial condition for aging, the presence of undissolved precipitates at micro-TiB_2 particles could induce certain detrimental effects during the subsequent aging behaviour. To distinguish the effect of a MS-ST on aging behaviour, single-step solution treatment (SS-ST) were performed.

A SS-ST was considered for two key reasons: (i) The presence of low-melting phases such as S-Al_2CuMg, Q-$Al_7Cu_3Mg_6$ in the AB state were not observed by any characterization technique. The

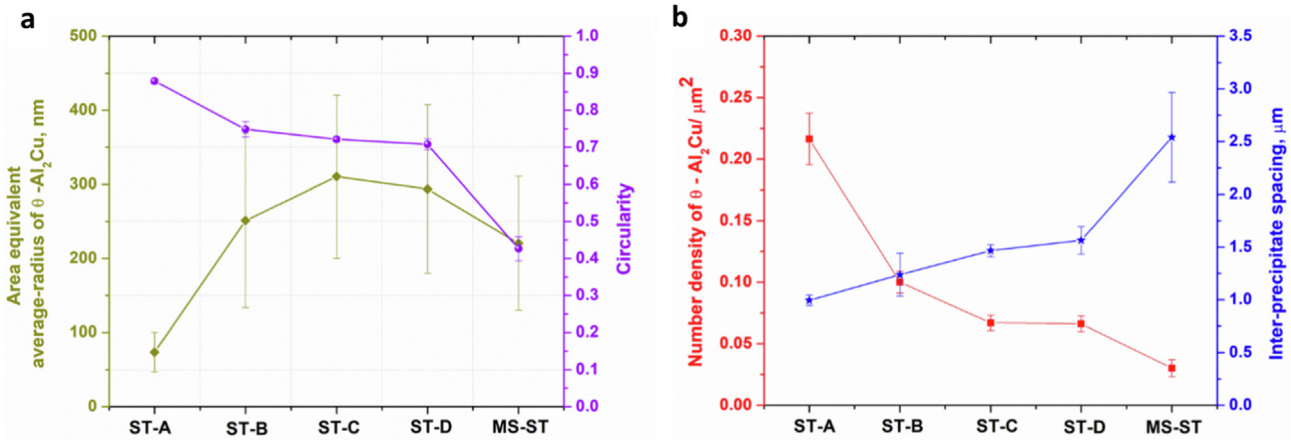

Fig. 11. Evolution of various features of θ-Al_2Cu precipitate as a function of interrupted solution steps showing (a) area equivalent average-radius and circularity and (b) number density and inter-precipitate spacing.

presence of such phases in the castings are the reason for performing long MS-ST to avoid incipient melting. However, in the LPBF processes, high cooling rates (~10^4-10^7 K/s) could supress the formation of these phases [19]. This allows applying only a single-step i.e. solutioning at 530 °C to dissolve θ-Al_2Cu eutectic, see Fig. 7**a**. (ii) It is quite evident now that, MS-ST allows migration and coarsening of θ-Al_2Cu near micro-TiB_2 particles which then become difficult to get completely dissolved even after holding at 530 °C for 12 h, see Fig. 10. Thus, a SS-ST could be able to avoid migration and subsequently coarsening of θ-Al_2Cu precipitates near micro-TiB_2 particles.

Solutioning time was optimized by comparing three-time intervals at 530 °C: 1 h, 6 h and 12 h. All the three conditions could be able to dissolve θ-Al_2Cu effectively, see supplementary **Fig S3**. However, solution treatment performed for 1 h was considered as it provides higher hardness.

After SS-ST (530 °C for 1 h), the sample was aged at 190 °C for 6 h and compared with MS-ST aged for 6 h i.e. PA state. These samples were named as SS-ST-A-6 h and PA (MS-ST-A-6 h) respectively. The comparative microstructural features were presented in terms of θ-Al_2Cu average size, area fraction and SEM-BSE micrographs (Fig. 12). A summary of these microstructural features is provided in Table 4. SS-ST-A-6 h possessed considerably lower average size and area fraction of θ-Al_2Cu precipitates than PA (MS-ST-A-6 h) as shown in Fig. 12**a**. In addition, a negligible fraction of θ-Al_2Cu precipitates were located near micro-TiB_2 particles, see Fig. 12**b** as compared with PA (MS-ST-A-6 h) **(**Fig. 12**c).** This indicates that most of the eutectic θ-Al_2Cu could be able to dissolve back into the Al-matrix in a SS-ST. Furthermore, the SS-ST avoids formation of blocky Al_2Cu phase near micro-TiB_2 particles unlike the case of the MS-ST **(**Fig. 10**).** The same was also confirmed from the phase quantification by Rietveld refinement, as shown in Table 4 and **Table S1**. SS-ST-A-6 h has around 0.9 wt% of Al_2Cu as compared to 1.9 wt% in PA (MS-ST-A-6 h).

Further characterization by HAADF-STEM of the SS-ST-A-6 h sample displayed grain boundary precipitates and grain interior needle-shaped precipitates, see Fig. 12**d** and Fig. 12**e**. These microstructural features are very similar to the PA (MS-ST-A-6 h) state, where the grain boundary precipitates are of equilibrium θ-Al_2Cu and the needle-shaped precipitates are of Ω and θ' **(**Fig. 8**).** The estimated dislocation density due to these matrix precipitates was comparable to the PA (MS-ST-A-6 h) state ≈ 4.67×10^{14}/ m^2 and the average length of the precipitates was 58 nm, although the distribution of precipitate length was bimodal, indicating the presence of some fine precipitates in SS-ST-A-6 h state **(**Fig. S2**c).** However, the PFZs width near micro-TiB_2 particles (≈ 32 nm) and near grain boundaries (≈ 43 nm) are opposite to that found in PA (MS-ST-A-6 h) state. The PFZs width was much higher near micro-TiB_2 than near grain boundaries in PA (MS-ST-A-6 h), see Fig. 8. This reduced PFZs width near micro-TiB_2 particles has been attributed to more complete dissolution of θ-Al_2Cu in single step solution treatment. As previously described the coarsening of θ-Al_2Cu near micro-TiB_2 particles in PA (MS-ST-A-6 h) can be associated with the presence of pre-existing θ-Al_2Cu precipitates near micro-TiB_2 particles. It is in fact well accepted that the presence of pre-existing precipitates accelerate the precipitation kinetics and showed a pronounced effect on the aging behaviour [65–67]. The θ-Al_2Cu coarsened preferentially at its pre-existing precipitates during secondary aging rather than nucleating as a new precipitate [66]. Rapid coarsening is detrimental to the materials mechanical as well as corrosion properties as it increases the PFZs width [67]. The width of PFZs plays a major role in grain boundary cracking in A20X alloy as a function of aging. Fig. 13 shows multiple grain boundary cracks in PA (MS-ST-A-6 h) whereas no such cracks were observed in SS-ST-A-6 h. Thus, the presence of pre-existing θ-Al_2Cu precipitates (Incomplete dissolution) after solution treatment alters the coarsening kinetics during aging and is undesirable in order to avoid early formation of PFZs.

3.6. Tensile behaviour

The mechanical behaviour of A20X alloy was tested for AB and PA (MS-ST-A-6 h) states. The results are shown as a tensile stress–strain curves in Fig. 14. Curve characteristics such as yield strength (YS), ultimate tensile strength (UTS) and total elongation to fracture (e %) are reported in Table 4 along with their microstructural features. The tensile behaviour of SS-ST-A-6 h state have also been shown for the comparison.

The AB sample possessed considerable strength (YS ≈ 304 MPa and UTS ≈ 378 MPa) and good ductility (e ≈ 12.5 %) with respect to an Al-metal matrix composites [68]. The tensile behaviour showed a typical stress–strain curve of an additive manufactured A20X alloy, displaying yield drop phenomena followed by inhomogeneous deformation (Lüders band formation and its spread) and strain hardening with serrated flow behaviour (Portevin-Le Chatelier -PLC effect) [27,28]. The PLC effect is due to repeated locking and unlocking of dislocations by solute atoms such as Cu and Mg. The high percentage of elongation to fracture in AB samples has been attributed to the strong bonding of micro- and nano-TiB_2 particles with the α-Al matrix [69].

The tensile curve of PA (MS-ST-A-6 h) samples showed a considerable increase in the strength but a reduced ductility with

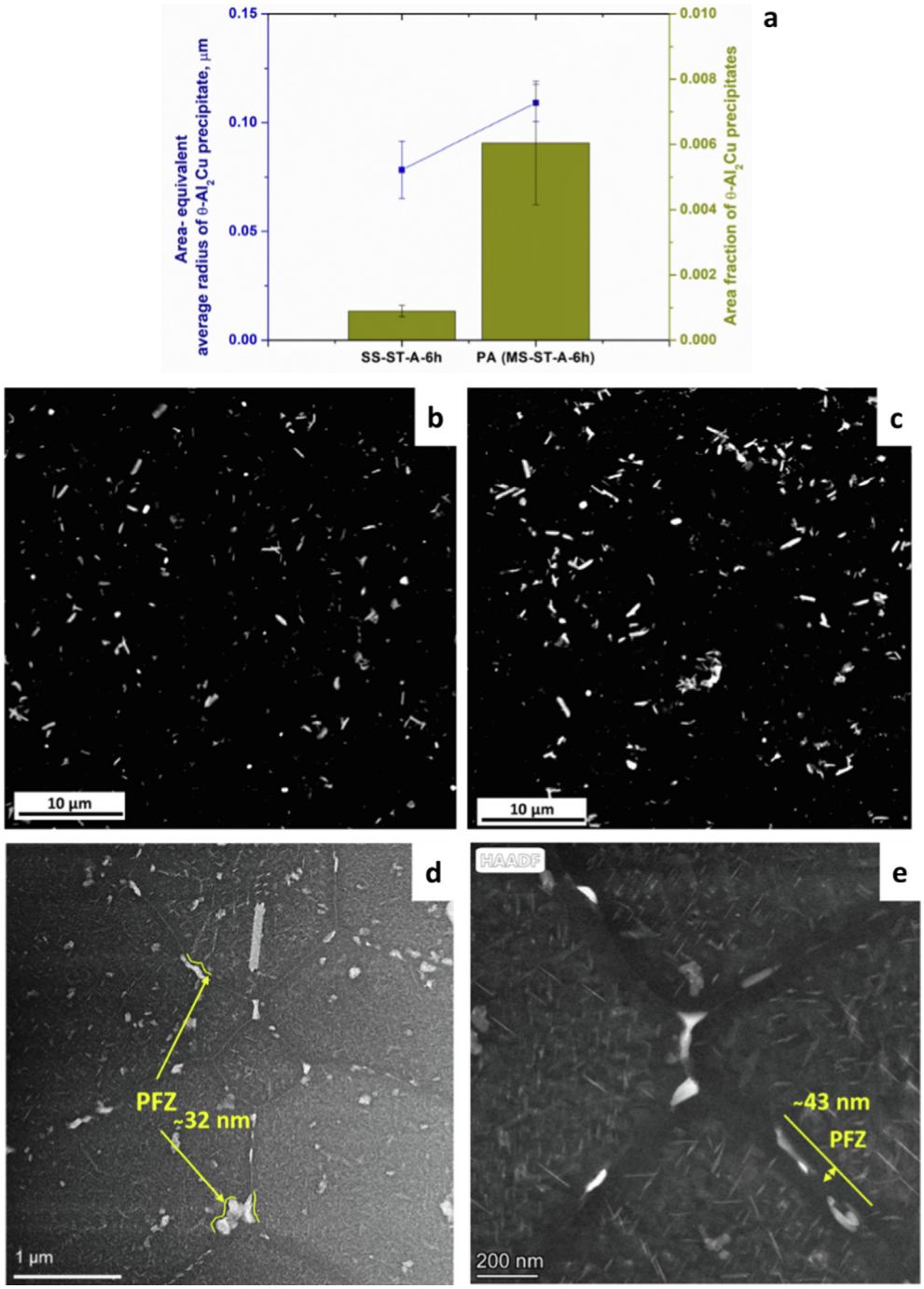

Fig. 12. (a) Area-equivalent average radius and area fraction of θ-Al_2Cu precipitates in SS-ST-A-6 h and PA (MS-ST-A-6 h); and their corresponding SEM-BSE micrographs under low brightness (b) SS-ST-A-6 h and (c) PA (MS-ST-A-6 h) *(TiB_2 particles as grey and θ-Al_2Cu as white)*. HAADF-STEM micrographs of SS-ST-A-6 h indicating PFZs, (d) near micro-TiB_2 particles and (e) near grain boundaries.

respect to AB samples. Unlike in the AB state, no serrated flow (PLC effect) was observed. It could be related to the consumption of solute atoms (Cu and Mg) in the formation of matrix precipitates such as Ω and θ' and precipitation of equilibrium θ-Al_2Cu during aging. Furthermore, Mg tends to segregate at the grain boundaries (Fig. 8). The YS and UTS values of PA (MS-ST-A-6 h) samples were 21 % and 15 % higher than the AB ones, respectively (Table 4). However, there was a significant loss in its ductility and the total elongation was drastically reduced to 58 % as that of the AB state. As compared to PA (MS-ST-A-6 h), the tensile curve of SS-ST-A-6 h demonstrated an improvement in both strength and ductility. The YS and UTS were increased by 7.1 % and 6.3 % respectively. Furthermore, the total elongation significantly increased by 45 % (Table 4). The reduced ductility in PA (MS-ST-A-6 h) state could be attributed to the presence of grain boundary cracks and creation of wide PFZs near micro-TiB_2 particles (Fig. 9). Although, grain boundary cracks have much severe effect on the ductility [56], PFZs possess less strength than grain boundaries which upon tensile loading results in formation of microcracks in these regions and propagate much easier causing a sudden failure [70,71].

Table 4
Summary of the mechanical properties and microstructural features at various heat treatment stages of LPBF manufactured A20X alloy.

Sample	Microstructural features						Mechanical properties			
	Average grain size, μm	θ-Al_2Cu, wt.%	Length of nano-precipitates (Ω/ θ'), nm	Dislocation density, x10^{14} /m^2	Width of PFZs, nm		Micro-hardness, HV	YS, MPa	UTS, MPa	e, %
					Near grain boundary	Near micro-TiB_2 particles				
AB	1.05 ± 0.4	4.2 ± 0.4	–	6.13 ± 0.32	–	–	113 ± 4	304 ± 3	378 ± 6	12.5 ± 1.6
MS-ST	1.97 ± 0.5	–	–	2.63 ± 0.27	–	–	103 ± 5	–	–	–
PA (MS-ST-A-6 h)	2.17 ± 0.5	1.9 ± 0.3	54 ± 17	5.34 ± 0.32	30 ± 6	85 ± 36	152 ± 6	370 ± 9	435 ± 13	7.3 ± 0.3
OA	1.93 ± 0.6	4.2 ± 0.3	82 ± 20 & 422 ± 63	4.14 ± 0.28	78 ± 7	153 ± 58	124 ± 5	–	–	–
SS-ST-A-6 h	–	0.9 ± 0.1	58 ± 25	4.67 ± 0.99	43 ± 8	32 ± 13	143 ± 2	396 ± 3	462 ± 4	10.6 ± 1.8

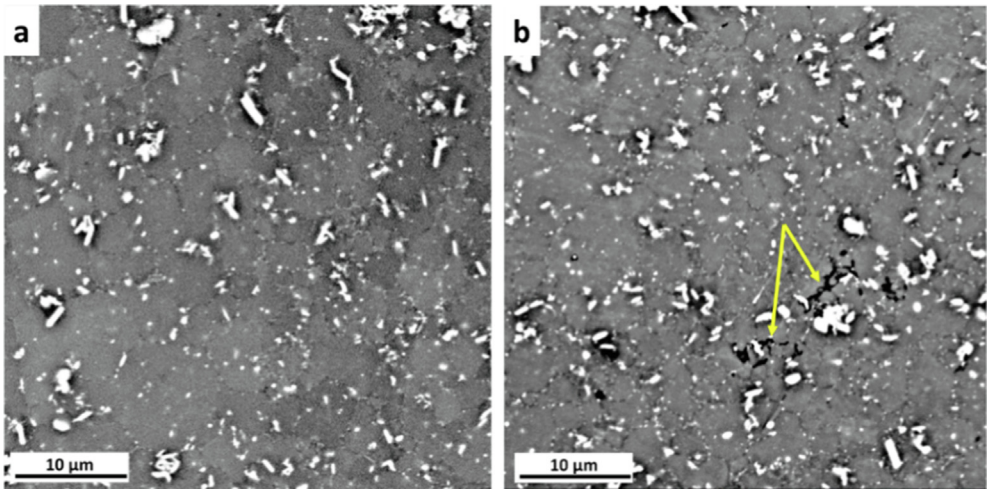

Fig. 13. SEM-BSE micrographs of (a) SS-ST-A-6 h and (b) PA (MS-ST-A-6 h) *(Yellow arrows depict grain boundary cracks)*. (For interpretation of the references to colour in this figure legend, the reader is referred to the web version of this article.)

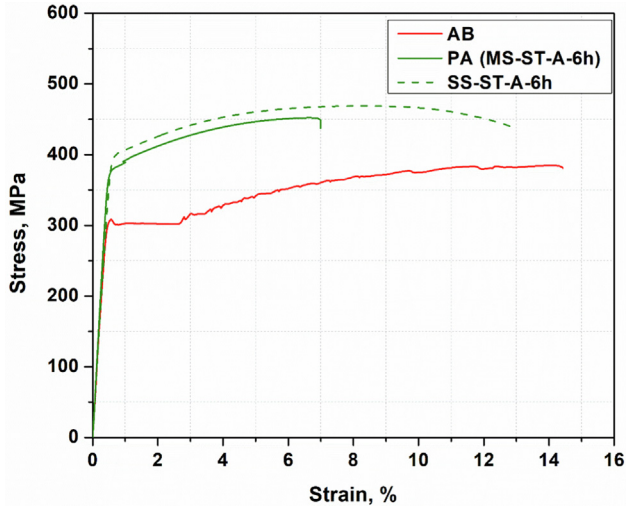

Fig. 14. Tensile stress–strain curves of A20X alloy in the AB, PA (MS-ST-A-6 h) and SS-ST-A-6 h conditions.

4. Conclusions

In this paper, the microstructural evolution of LPBF A20X samples during a T7 post-processing heat treatment was investigated. Initially, the microstructural evolution was considered for four main states: as-built (AB), multi-step solution treatment (MS-ST), peak aged (PA) and over aged (OA). Then, the microstructural evolution of multi-step solution treatment was done at various interrupted solution steps. Post to the microstructural analysis, a short and simple heat treatment was proposed and compared with T7 in terms of microstructure and mechanical behaviour. The key results of this investigation are as follows:

1. The A20X AB microstructure was similar to the microstructure of the as-atomized powder. It was composed of fine cellular structures with α-Al cells and θ-Al_2Cu eutectic as cell boundaries. The mirco-TiB_2 particles were present at triple junctions, within the cells as well as at the cell boundaries. MS-ST dissolved the eutectic θ-Al_2Cu and solutionized Al matrix with Cu.
2. The PA state was characterized by θ-Al_2Cu precipitates near the micro- and nano-TiB_2 particles (present specifically at grain boundaries), this is due to the difference in coefficient of thermal expansion between Al (matrix) and TiB_2 (reinforcement). Excessive aging (OA) resulted in significant growth of θ-Al_2Cu precipitates and engulfment of micro-TiB_2 particles. PA and OA microstructures displayed grain boundary cracks which were more severe in the case of OA state.
3. The origin of grain boundary cracking has been associated to the synergetic effect of micro-strains developed due to precipitation of Ω and θ' at grain interiors and simultaneous widening of PFZs near grain boundaries and near micro-TiB_2 particles.
4. The key microstructural features responsible for PA hardness are; (i) presence of coherent-Ω and semi-coherent-θ' matrix precipitates of nano-size (about 54 nm in length) and are considered as one of the strengthening phases, (ii) optimum precipitation of θ-Al_2Cu precipitates and (iii) less frequent grain boundary cracks than OA state.

5. The microstructural evolution of MS-ST revealed that the low temperature solution steps caused break-up of θ-Al_2Cu eutectic network into fine and spheroidal particles that migrated towards micro-TiB_2 particles and coarsened. Additionally, it was pointed out that the very long MS-ST leads to an incomplete dissolution of θ-Al_2Cu. This has been attributed to the shielding effect of TiB_2 particles between θ-Al_2Cu and α-Al matrix which limits the θ-Al_2Cu dissolution.
6. The proposed single-step solution treatment (SS-ST) allowed a nearly complete dissolution of θ-Al_2Cu. The microstructure of SS-ST aged for 6 h revealed negligible precipitation of θ-Al_2Cu near micro-TiB_2 particles, the width of PFZs near micro-TiB_2 particles (≈ 32 nm) was much less than in the MS-ST aged for 6 h (≈ 85 nm), and thus, no grain boundary cracks were observed in SS-ST aged for 6 h.
7. The mechanical behaviour of AB, PA (MS-ST-A-6 h) and SS-ST-A-6 h were compared. The AB specimen displayed a typical tensile curve with Lüders band formation and PLC effect. PA (MS-ST-A-6 h) showed 21 % and 15 % increase in YS and UTS respectively as compared to the AB state and a reduction of elongation to fracture by 58 %. No PLC effect was observed in PA (MS-ST-A-6 h) state. On the other hand, SS-ST-A-6 h demonstrated a significant increase in elongation to fracture by 45 % with respect to PA (MS-ST-A-6 h). The YS and UTS increased by 7.1 % and 6.3 % respectively. The improved strength and ductility in SS-ST-A-6 h has been attributed to the absence of grain boundary cracks.

Based on the current investigation, the proposed post-processing heat treatment for the AM printed A20X alloy offers better mechanical properties than the conventional T7. It is short and simple, energy efficient and can be easily adaptable for the industrial practices.

Data availability

Data will be made available on request.

Declaration of Competing Interest

The authors declare that they have no known competing financial interests or personal relationships that could have appeared to influence the work reported in this paper.

Acknowledgement

The authors would like to acknowledge the European research project MANUELA Additive Manufacturing using Metal Pilot Line (Project ID 820774) which received funding from the European Union's Horizon2020 research and innovation program. The authors would like to thank Mr. Dario Pezzini for carrying out the tensile test and Ms. Irene Abbona for the support with experimental analysis. The presented investigations were carried out at RWTH Aachen University within the framework of the Collaborative Research Centre SFB1120-236616214 "Bauteilpräzision durch Beherrschung von Schmelze und Erstarrung in Produktionsprozessen" and funded by the Deutsche For-schungsgemeinschaft e.V. (DFG, German Research Foundation). The sponsorship and support are gratefully acknowledged.

Appendix A. Supplementary material

Supplementary data to this article can be found online at https://doi.org/10.1016/j.matdes.2022.111566.

References

[1] W.E. Frazier, Metal additive manufacturing: a review, J. Mater. Eng. Perform. 23 (2014) 1917–1928, https://doi.org/10.1007/s11665-014-0958-z.
[2] T. DebRoy, H.L. Wei, J.S. Zuback, T. Mukherjee, J.W. Elmer, J.O. Milewski, A.M. Beese, A.D. Wilson-Heid, A. De, W. Zhang, Additive manufacturing of metallic components–process, structure and properties, Prog. Mater. Sci. 92 (2018) 112–224, https://doi.org/10.1016/j.pmatsci.2017.10.001.
[3] M.C. Brennan, J.S. Keist, T.A. Palmer, Defects in metal additive manufacturing processes, J. Mater. Eng. Perform. 30 (2021) 4808–4818, https://doi.org/10.1007/s11665-021-05919-6.
[4] A.T. Erturk, M.E. Bulduk, G. Tarakçi, G. Özer, E. Yarar, Investigation of the microstructure and mechanical characteristics of lattice structures produced by laser powder bed fusion method, Met. Mater. Int. 28 (2022) 155–167, https://doi.org/10.1007/s12540-021-01038-y.
[5] G. Özer, G. Tarakçi, M.S. Yilmaz, Z. Öter, Ö. Sürmen, Y. Akça, M. Coşkun, E. Koç, Investigation of the effects of different heat treatment parameters on the corrosion and mechanical properties of the AlSi10Mg alloy produced with direct metal laser sintering, Mater. Corros. 71 (2020) 365–373, https://doi.org/10.1002/maco.201911171.
[6] J. Fiocchi, A. Tuissi, C.A. Biffi, Heat treatment of aluminium alloys produced by laser powder bed fusion: a review, Mater. Des. 204 (2021), https://doi.org/10.1016/j.matdes.2021.109651.
[7] C. Li, Z.Y. Liu, X.Y. Fang, Y.B. Guo, Residual stress in metal additive manufacturing, Procedia CIRP. 71 (2018) 348–353, https://doi.org/10.1016/j.procir.2018.05.039.
[8] AMS AM Additive Manufacturing Metals, Aluminum Alloy Powder 4.6Cu - 3.4Ti - 1.4B - 0.75Ag - 0.27Mg, SAE International, 2021. https://doi.org/10.4271/AMS7033.
[9] A. Aversa, P. Fino, Special issue on materials development by additive manufacturing techniques, Appl. Sci. 10 (2020) 2–5, https://doi.org/10.3390/app10155119.
[10] S.A. Butler, An aluminium-copper alloy, GB2334966A, UK Patent, 2003.
[11] H.R. Kotadia, G. Gibbons, A. Das, P.D. Howes, A review of laser powder bed fusion additive manufacturing of aluminium alloys: microstructure and properties, Addit. Manuf. 46 (2021), https://doi.org/10.1016/j.addma.2021.102155 102155.
[12] J.H. Martin, B.D. Yahata, J.M. Hundley, J.A. Mayer, T.A. Schaedler, T.M. Pollock, 3D printing of high-strength aluminium alloys, Nature. 549 (2017) 365–369, https://doi.org/10.1038/nature23894.
[13] I.J. Polmear, M.J. Couper, Design and development of an experimental wrought aluminum alloy for use at elevated temperatures, Metall. Trans. A. 19 (1988) 1027–1035, https://doi.org/10.1007/BF02628387.
[14] S.P. Ringer, K. Hono, I.J. Polmear, T. Sakurai, Nucleation of precipitates in aged AlCuMg (Ag) alloys with high Cu: Mg ratios, Acta Mater. 44 (1996) 1883–1898, https://doi.org/10.1016/1359-6454(95)00314-2.
[15] A. Kordijazi, D. Weiss, Effect of solidification time on microstructure, wettability, and corrosion properties of A205–T7 aluminum alloys, Int. J. Met. 15 (2021) 2–12, https://doi.org/10.1007/s40962-020-00457-8.
[16] E.P. Masuku, G. Govender, L. Ivanchev, H. Möller, Rheocasting of Al-Cu alloy A201 with different silver contents, Solid State Phenom. 141–143 (2008) 151–156, https://doi.org/10.4028/www.scientific.net/ssp.141-143.151.
[17] H. Möller, G. Govender, The heat treatment of rheo-high pressure die cast Al-Cu-Mg-Ag alloy 2139, Solid State Phenom. 192–193 (2013) 173–178, https://doi.org/10.4028/www.scientific.net/SSP.192-193.173.
[18] P. Daswa, H. Möller, G. Govender, Optimization of the solution heat treatment of rheo-high pressure die cast Al-Cu-Mg-Ag 2139 alloy, Mater. Sci. Forum. 828–829 (2015) 226–231, https://doi.org/10.4028/www.scientific.net/MSF.828-829.226.
[19] M. Zamani, S. Toschi, A. Morri, L. Ceschini, S. Seifeddine, Optimisation of heat treatment of Al–Cu–(Mg–Ag) cast alloys, J. Therm. Anal. Calorim. 139 (2020) 3427–3440, https://doi.org/10.1007/s10973-019-08702-x.
[20] M. Avateffazeli, P.E. Carrion, B. Shachi-Amirkhiz, H. Pirgazi, M. Mohammadi, N. Shamsaei, M. Haghshenas, Correlation between tensile properties, microstructure, and processing routes of an Al–Cu–Mg–Ag–TiB2 (A205) alloy: additive manufacturing and casting, Mater. Sci. Eng. A. 841 (2022), https://doi.org/10.1016/j.msea.2022.142989 142989.
[21] S.I. Shakil, A.S. Zoeram, H. Pirgazi, B. Shalchi-Amirkhiz, B. Poorganji, M. Mohammadi, M. Haghshenas, Microstructural-micromechanical correlation in an Al–Cu–Mg–Ag–TiB2 (A205) alloy: additively manufactured and cast, Mater. Sci. Eng. A. 832 (2022), https://doi.org/10.1016/j.msea.2021.142453 142453.
[22] J. Mayer, L.A. Giannuzzi, T. Kamino, J. Michael, TEM sample preparation and FIB-induced damage, MRS Bull. 32 (2007) 400–407, https://doi.org/10.1557/mrs2007.63.
[23] A. Kovács, R. Schierholz, K. Tillmann, FEI Titan G2 80–200 CREWLEY, J. Large-Scale Res. Facil. JLSRF. 2 (2016) A43–A.
[24] G.K. Williamson, R.E. Smallman III, Dislocation densities in some annealed and cold-worked metals from measurements on the X-ray Debye-Scherrer spectrum, Philos. Mag. 1 (1956) 34–46, https://doi.org/10.1080/14786435608238074.
[25] N. Naga Krishna, R. Tejas, K. Sivaprasad, K. Venkateswarlu, Study on cryorolled Al-Cu alloy using X-ray diffraction line profile analysis and evaluation of strengthening mechanisms, Mater. Des. 52 (2013) 785–790, https://doi.org/10.1016/j.matdes.2013.05.095.
[26] T. Liu, J.D. Leazer, S.K. Menon, L.N. Brewer, Microstructural analysis of gas atomized Al-Cu alloy feedstock powders for cold spray deposition, Surf.

Coatings Technol. 350 (2018) 621–632, https://doi.org/10.1016/j.surfcoat.2018.07.006.
[27] P. Mair, L. Kaserer, J. Braun, N. Weinberger, I. Letofsky-Papst, G. Leichtfried, Microstructure and mechanical properties of a TiB2-modified Al–Cu alloy processed by laser powder-bed fusion, Mater. Sci. Eng. A. 799 (2021), https://doi.org/10.1016/j.msea.2020.140209 140209.
[28] M.H. Ghoncheh, M. Sanjari, A.S. Zoeram, E. Cyr, B.S. Amirkhiz, A. Lloyd, M. Haghshenas, M. Mohammadi, On the microstructure and solidification behavior of new generation additively manufactured Al-Cu-Mg-Ag-Ti-B alloys, Addit. Manuf. 37 (2021), https://doi.org/10.1016/j.addma.2020.101724 101724.
[29] E.A. Jägle, Z. Sheng, L. Wu, L. Lu, J. Risse, A. Weisheit, D. Raabe, Precipitation reactions in age-hardenable alloys during laser additive manufacturing, JOM. 68 (2016) 943–949, https://doi.org/10.1007/s11837-015-1764-2.
[30] S.K. Varma, D. Salas, E. Corral, E. Esquivel, K.K. Chawla, R. Mahapatra, Microstructural development during aging of, aluminum alloy composite, J. Mater. Sci. 34 (1999) (2014) 1855–1863, https://doi.org/10.1023/A:1004527729424.
[31] C. Bartels, D. Raabe, G. Gottstein, U. Huber, Investigation of the precipitation kinetics in an A16061/TiB2 metal matrix composite, Mater. Sci. Eng. A. 237 (1997) 12–23, https://doi.org/10.1016/S0921-5093(97)00104-4.
[32] A. Mandal, R. Maiti, M. Chakraborty, B.S. Murty, Effect of TiB2 particles on aging response of Al–4Cu alloy, Mater. Sci. Eng. A. 386 (2004) 296–300, https://doi.org/10.1016/j.msea.2004.07.026.
[33] I. Dutta, D.L. Bourell, A theoretical and experimental study of aluminum alloy 6061-SiC metal matrix composite to identify the operative mechanism for accelerated aging, Mater. Sci. Eng. A. 112 (1989) 67–77, https://doi.org/10.1016/0921-5093(89)90345-6.
[34] T. Christman, A. Needleman, S. Nutt, S. Suresh, On microstructural evolution and micromechanical modelling of deformation of a whisker-reinforced metal-matrix composite, Mater. Sci. Eng. A. 107 (1989) 49–61, https://doi.org/10.1016/0921-5093(89)90374-2.
[35] M. Pa, M. Ferry, T. Chandra, Five decades of the Zener equation, ISIJ Int. 38 (1998) 913–924, https://doi.org/10.2355/isijinternational.38.913.
[36] S. Marola, D. Gianoglio, F. Bosio, A. Aversa, M. Lorusso, D. Manfredi, M. Lombardi, L. Battezzati, Alloying AlSi10Mg and Cu powders in laser Single Scan Tracks, melt spinning, and Laser Powder Bed Fusion, J. Alloys Compd. 821 (2020), https://doi.org/10.1016/j.jallcom.2019.153538 153538.
[37] N.T. Aboulkhair, M. Simonelli, L. Parry, I. Ashcroft, C. Tuck, R. Hague, 3D printing of Aluminium alloys: additive Manufacturing of Aluminium alloys using selective laser melting, Prog. Mater. Sci. 106 (2019), https://doi.org/10.1016/j.pmatsci.2019.100578 100578.
[38] J. Wang, Z. Liu, S. Bai, J. Cao, J. Zhao, L. Luo, J. Li, Microstructure evolution and mechanical properties of the electron-beam welded joints of cast Al–Cu–Mg–Ag alloy, Mater. Sci. Eng. A. 801 (2021), https://doi.org/10.1016/j.msea.2020.140363 140363.
[39] I. Zuiko, R. Kaibyshev, Aging behavior of an Al–Cu–Mg alloy, J. Alloys Compd. 759 (2018) 108–119, https://doi.org/10.1016/j.jallcom.2018.05.053.
[40] X.J. Jiang, B. Noble, B. Holme, G. Waterloo, J. Tafto, Differential scanning calorimetry and electron diffraction investigation on low-temperature aging in Al-Zn-Mg alloys, Metall. Mater. Trans. A Phys. Metall. Mater. Sci. 31 (2000) 339–348, https://doi.org/10.1007/s11661-000-0269-x.
[41] L.D.E.L. Castillo, E.J. Lavernia, Microstructure and Mechanical Behavior of Spray-Deposited Al-Cu-Mg (-Ag-Mn), Alloys 31 (2000) 2287–2298, https://doi.org/10.1007/s11661-000-0145-8.
[42] X.Y. Liu, Q.L. Pan, L.Y. Zheng, Q.R. Fu, F. Gao, M.X. Li, Y.M. Bai, Effect of aging temper on the thermal stability of Al–Cu–Mg–Ag heat-resistant alloy, Mater. Des. 46 (2013) 360–365, https://doi.org/10.1016/j.matdes.2012.10.039.
[43] K. Hono, T. Sakurai, I.J. Polmear, Pre-precipitate clustering in an AlCuMgAg alloy, Scr. Metall. Mater. 30 (1994) 695–700, https://doi.org/10.1016/0956-716X(94)90184-8.
[44] D. Bakavos, P.B. Prangnell, B. Bes, F. Eberl, The effect of silver on microstructural evolution in two 2xxx series Al-alloys with a high Cu: Mg ratio during ageing to a T8 temper, Mater. Sci. Eng. A. 491 (2008) 214–223, https://doi.org/10.1016/j.msea.2008.03.014.
[45] D.H. Xiao, J.N. Wang, D.Y. Ding, S.P. Chen, Effect of Cu content on the mechanical properties of an Al–Cu–Mg–Ag alloy, J. Alloys Compd. 343 (2002) 77–81, https://doi.org/10.1016/S0925-8388(02)00076-2.
[46] S. Bai, X. Zhou, Z. Liu, P. Xia, M. Liu, S. Zeng, Effects of Ag variations on the microstructures and mechanical properties of Al–Cu–Mg alloys at elevated temperatures, Mater. Sci. Eng. A. 611 (2014) 69–76, https://doi.org/10.1016/j.msea.2014.05.065.
[47] C.R. Hutchinson, X. Fan, S.J. Pennycook, G.J. Shiflet, On the origin of the high coarsening resistance of Ω plates in Al–Cu–Mg–Ag alloys, Acta Mater. 49 (2001) 2827–2841, https://doi.org/10.1016/S1359-6454(01)00155-0.
[48] M. Gazizov, R. Kaibyshev, Precipitation structure and strengthening mechanisms in an Al-Cu-Mg-Ag alloy, Mater. Sci. Eng. A. 702 (2017) 29–40, https://doi.org/10.1016/j.msea.2017.06.110.
[49] Y, Gazizova, R.O, Kaibyshev, Materials Characterization Precipitate / matrix incompatibilities related to the { 111 } Al Ω plates in an Al-Cu-Mg-Ag alloy, 182 (2021). https://doi.org/https://doi.org/10.1016/j.matchar.2021.111586.
[50] S.J. Kang, Y.W. Kim, M. Kim, J.M. Zuo, Determination of interfacial atomic structure, misfits and energetics of Ω phase in Al-Cu-Mg-Ag alloy, Acta Mater. 81 (2014) 501–511, https://doi.org/10.1016/j.actamat.2014.07.074.
[51] K. Kim, B.C. Zhou, C. Wolverton, Interfacial stability of θ′/Al in Al-Cu alloys, Scr. Mater. 159 (2019) 99–103, https://doi.org/10.1016/j.scriptamat.2018.09.018.
[52] V. Vaithyanathan, C. Wolverton, L.Q. Chen, Multiscale modeling of θ′ precipitation in Al-Cu binary alloys, Acta Mater. 52 (2004) 2973–2987, https://doi.org/10.1016/j.actamat.2004.03.001.
[53] J.E. Franklin, W.F. Savage, Stress Relaxation and Strain-Age Cracking in Rene 41 Weldments, Weld. J. 53 (1974) 380–387. http://aws.perusion.com/wj/supplement/WJ_1974_09_s380.pdf.
[54] F. Hanning, G. Singh, J. Andersson, The effect of grain size on the susceptibility towards strain age cracking of wrought haynes® 282®, Adv. Transdiscipl. Eng. 13 (2020) 407–416, https://doi.org/10.3233/ATDE200178.
[55] A.W. Dix, W.F. Savage, Factors influencing strain-age cracking in Inconel X-750, Weld. J. 50 (1971) 247. http://files.aws.org/wj/supplement/WJ_1971_06_s247.pdf.
[56] G. Itoh, M. Kanno, T. Hagiwara, T. Sakamoto, Embrittlement in an age-hardened 2091 aluminum alloy by exposure at elevated temperatures below the aging temperature, Acta Mater. 47 (1999) 3799–3809, https://doi.org/10.1016/S1359-6454(99)00243-8.
[57] M. Fourmeau, C.D. Marioara, T. Børvik, A. Benallal, O.S. Hopperstad, A study of the influence of precipitate-free zones on the strain localization and failure of the aluminium alloy AA7075-T651, Philos. Mag. 95 (2015) 3278–3304, https://doi.org/10.1080/14786435.2015.1040099.
[58] G. Sharma, R.V. Ramanujan, G.P. Tiwari, Instability mechanisms in lamellar microstructures, Acta Mater. 48 (2000) 875–889, https://doi.org/10.1016/S1359-6454(99)00378-X.
[59] J.C.M. Kampe, T.H. Courtney, Y. Leng, Shape instabilities of plate-like structures-I, Experimental observations in heavily cold worked in situ composites, Acta Metall. 37 (1989) 1735–1745, https://doi.org/10.1016/0001-6160(89)90059-X.
[60] R.D. Vengrenovitch, On the ostwald ripening theory, Acta Metall. 30 (1982) 1079–1086, https://doi.org/10.1016/0001-6160(82)90004-9.
[61] M. Zamani, I. Belov, E. Sjölander, A. Bjurenstedt, E. Ghassemali, S. Seifeddine, Study on dissolution of Al2Cu in al-4.3 cu and a205 cast alloys, Metals (Basel) 10 (2020) 900, https://doi.org/10.3390/met10070900.
[62] A. Lombardi, D. Sediako, C. Ravindran, M. Barati, Analysis of precipitation, dissolution and incipient melting of Al2Cu in B206 Al alloy using in-situ neutron diffraction, J. Alloys Compd. 784 (2019) 1017–1025, https://doi.org/10.1016/j.jallcom.2019.01.104.
[63] J. Geng, T. Hong, Y. Ma, M. Wang, D. Chen, N. Ma, H. Wang, The solution treatment of in-situ sub-micron TiB2/2024 Al composite, Mater. Des. 98 (2016) 186–193, https://doi.org/10.1016/j.matdes.2016.03.024.
[64] Z. Asghar, G. Requena, H.P. Degischer, P. Cloetens, Three-dimensional study of Ni aluminides in an AlSi12 alloy by means of light optical and synchrotron microtomography, Acta Mater. 57 (2009) 4125–4132, https://doi.org/10.1016/j.actamat.2009.05.010.
[65] Q. Zhang, X. Luan, S. Dhawan, D.J. Politis, Q. Du, M.W. Fu, K. Wang, M.M. Gharbi, L. Wang, Development of the post-form strength prediction model for a highstrength 6xxx aluminium alloy with pre-existing precipitates and residual dislocations, Int. J. Plast. 119 (2019) 230–248, https://doi.org/10.1016/j.ijplas.2019.03.013.
[66] J. Buha, R.N. Lumley, A.G. Crosky, K. Hono, Secondary precipitation in an Al-Mg-Si-Cu alloy, Acta Mater. 55 (2007) 3015–3024, https://doi.org/10.1016/j.actamat.2007.01.006.
[67] P. Sepehrband, R. Mahmudi, F. Khomamizadeh, Effect of Zr addition on the aging behavior of A319 aluminum cast alloy, Scr. Mater. 52 (2005) 253–257, https://doi.org/10.1016/j.scriptamat.2004.10.025.
[68] S. Tang, R. Ummethala, C. Suryanarayana, J. Eckert, K.G. Prashanth, Z. Wang, Additive manufacturing of aluminum-based metal matrix composites—a review, Adv. Eng. Mater. 23 (2021) 1–17, https://doi.org/10.1002/adem.202100053.
[69] X.P. Li, G. Ji, Z. Chen, A. Addad, Y. Wu, H.W. Wang, J. Vleugels, J. Van Humbeeck, J.P. Kruth, Selective laser melting of nano-TiB2decorated AlSi10Mg alloy with high fracture strength and ductility, Acta Mater. 129 (2017) 183–193, https://doi.org/10.1016/j.actamat.2017.02.062.
[70] M. de Haas, S.M. van Scherpenzeel, J.T.M. de Hosson, Grain boundary segregation and precipitation in aluminium Alloy AA6061, Mater. Sci. Forum. 519–521 (2006) 467–472, https://doi.org/10.4028/www.scientific.net/msf.519-521.467.
[71] T. Pardoen, D. Dumont, A. Deschamps, Y. Brechet, Grain boundary versus transgranular ductile failure, J. Mech. Phys. Solids. 51 (2003) 637–665, https://doi.org/10.1016/S0022-5096(02)00102-3.